

# HCl Oxidation on $\text{IrO}_2$ -Based Catalysts: From Fundamentals to Scale-Up

Maximilian Moser,<sup>†</sup> Cecilia Mondelli,<sup>†</sup> Amol P. Amrute,<sup>†</sup> Atsushi Tazawa,<sup>†</sup> Detre Teschner,<sup>‡</sup> Manfred E. Schuster,<sup>‡</sup> Achim Klein-Hoffman,<sup>‡</sup> Núria López,<sup>§</sup> Timm Schmidt,<sup>||</sup> and Javier Pérez-Ramírez\*,<sup>†</sup>

<sup>†</sup>Institute for Chemical and Bioengineering, Department of Chemistry and Applied Biosciences, ETH Zurich, Wolfgang-Pauli-Strasse 10, CH-8093 Zurich, Switzerland

<sup>‡</sup>Fritz-Haber-Institute of the Max Planck Society, Faradayweg 4-6, D-14159 Berlin, Germany

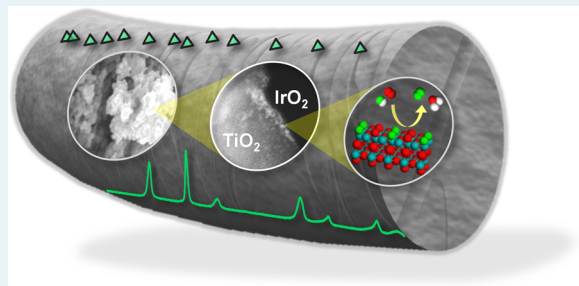
<sup>§</sup>Institute of Chemical Research of Catalonia (ICIQ), Av. Països Catalans 16, 43007 Tarragona, Spain

<sup>||</sup>Bayer MaterialScience AG, IO-BC-T&I, K12, Chempark, K12, D-51368, Leverkusen, Germany

## Supporting Information

**ABSTRACT:**  $\text{IrO}_2$  has been investigated as alternative rutile-type catalyst to  $\text{RuO}_2$  for gas-phase HCl oxidation. The HCl conversion level over  $\text{IrO}_2$  at 723 K was comparable to that of  $\text{RuO}_2$  at ca. 170 K lower temperature, in line with the higher computed energy barrier for chlorine evolution over the former oxide. Similarly to  $\text{RuO}_2$ , chlorination took place only at the  $\text{IrO}_2$  surface, which is predicted to exhibit full occupation of the coordinatively unsaturated iridium sites and replacement of 50% of the oxygen bridge positions by chlorine. Advantageously,  $\text{IrO}_2$  is more resistant than  $\text{RuO}_2$  against oxidation, since the latter forms volatile  $\text{RuO}_4$  species at high temperatures.  $\text{IrO}_2$  (2 wt %) supported on  $\text{TiO}_2$ -rutile displayed a 6 times higher activity than on  $\text{TiO}_2$ -anatase. Although this corroborates the crucial role of the structural similarity between the carrier and active phase highlighted in the development of  $\text{RuO}_2$ -based catalysts, some differences were uncovered. (i) Small and highly dispersed  $\text{IrO}_2$  clusters rather than thin films are present on  $\text{TiO}_2$ -rutile, in line with the expected preference for Stranski-Krastanov-type growth rather than epitaxial growth due to strain. (ii) Geometric and electronic effects of  $\text{TiO}_2$ -rutile are predicted not to lead to improved HCl oxidation activity for 1 and 2 epilayers of  $\text{IrO}_2$  over the carrier. (iii) The superior performance of  $\text{IrO}_2/\text{TiO}_2$ -rutile thus mainly originates from the higher metal dispersion. A rational approach was applied to manufacture this catalyst in technical form. The successful protocol comprised  $\text{TiO}_2$ -anatase-aided extrusion of the rutile support followed by metal impregnation. The catalytic activity and kinetic fingerprints were unaltered upon shaping, and its robustness was highlighted in a 50 h test. On the basis of these findings,  $\text{IrO}_2/\text{TiO}_2$ -rutile represents a suitable high-temperature HCl oxidation catalyst that could be applied in staged fixed-bed reactors along with the low-temperature  $\text{RuO}_2$ -based materials.

**KEYWORDS:** HCl oxidation, chlorine,  $\text{IrO}_2$ ,  $\text{TiO}_2$ , DFT, scale up, technical catalyst



## 1. INTRODUCTION

After a long history of vain attempts to develop active and stable catalysts for gas-phase HCl oxidation, the last two decades have witnessed the crystallization of research efforts into robust  $\text{RuO}_2$ -based catalytic technologies.<sup>1,2</sup> These have been successfully applied at the large scale for the recycling of chlorine from byproduct HCl streams of phosgenation processes (i.e., polyurethane and polycarbonate manufacturing).<sup>1</sup> The superiority of  $\text{RuO}_2$ -based materials is related to the outstanding low-temperature activity of  $\text{RuO}_2$  and its resistance against bulk chlorination.<sup>3,4</sup> Rutile-type  $\text{TiO}_2$  and  $\text{SnO}_2$  oxides have been identified as the best supports because  $\text{RuO}_2$  is deposited in the form of epitaxially grown structures as a result of lattice matching, leading to enhanced dispersion and stabilization of the active phase.<sup>5,6</sup> However, due to the temperature rise associated with the exothermicity of the

reaction,  $\text{RuO}_2$  sintering may occur after long-term use. This can be minimized by incorporation of additives to the catalysts.<sup>5,7</sup> Still, if the temperature exceeds ca. 673 K, volatilization of  $\text{RuO}_2$  in form of  $\text{RuO}_4$  becomes possible.<sup>8</sup> This phenomenon has been reported as the cause of notable activity deterioration during long-term operation at 773 K.<sup>9</sup> Therefore, the current HCl oxidation processes could be further improved if alternative high-temperature catalysts were available.

$\text{IrO}_2$  attracted our attention mainly because of its structural similarity to  $\text{RuO}_2$ . From a fundamental viewpoint, it would be interesting to assess whether rutile-type oxides exhibit similar

Received: July 14, 2013

Revised: October 16, 2013

Published: October 17, 2013

Deacon chemistry. Furthermore, from the perspective of developing a catalyst for practical use, this would also enable an evaluation of whether the main catalyst design strategy at the basis of the superior performance of technical  $\text{RuO}_2$ -based catalysts, namely, the lattice matching with the carrier, can be transferred to other active rutile phases. A theoretical study by Studt et al.<sup>10</sup> simulated the oxidation of HCl on  $\text{IrO}_2(110)$ , predicting a significantly inferior activity compared with  $\text{RuO}_2(110)$  due to a highly endergonic atomic chlorine recombination over the former oxide. These results were based on the typical operating temperature of  $\text{RuO}_2$  (573 K) and have not been verified experimentally to date. Promising indications arise from the field of electrocatalytic oxidation of HCl to  $\text{Cl}_2$ , where  $\text{IrO}_2$  has been identified as the only electronically conducting material under oxygen and chlorine evolution reaction conditions besides  $\text{RuO}_2$ .<sup>11</sup> Dimensionally stable anodes (DSAs) constructed with  $\text{IrO}_2$  exhibit a slightly inferior activity compared with  $\text{RuO}_2$ -based DSAs but a much greater resistance to dissolution in the highly acidic environment. Accordingly,  $\text{IrO}_2$  is commonly added to the  $\text{RuO}_2$  anode coating, mostly in a molar 1:1 ratio of the oxides, to improve the service lifetime in the chlor-alkali industry.<sup>11</sup>

Herein we elucidate the HCl oxidation properties of bulk  $\text{IrO}_2$  in terms of activity, stability, kinetics, and mechanism. Subsequently, it is shown that a much better performing catalyst is obtained supporting  $\text{IrO}_2$  on  $\text{TiO}_2$ -rutile rather than on  $\text{TiO}_2$ -anatase, confirming the crucial role of the lattice matching between active phase and support to attain a superior dispersion. Finally, our optimal supported catalyst is scaled up into extrudate form. We demonstrate that the technical  $\text{IrO}_2$ / $\text{TiO}_2$ -rutile system represents a suitable high-temperature HCl oxidation catalytic technology complementary to that of low-temperature  $\text{RuO}_2$ -based catalysts.

## 2. EXPERIMENTAL SECTION

**2.1. Catalysts.** Bulk  $\text{IrO}_2$  and  $\text{RuO}_2$  catalysts were obtained by static-air calcination of anhydrous  $\text{IrCl}_3$  (ABCR, 99.9%) and  $\text{RuCl}_3$  (Alfa Aesar, 99.99%), respectively, at 823 K for 5 h using a heating rate of 5 K min<sup>-1</sup>. Supported  $\text{IrO}_2$  catalysts (nominal 1–10 wt % Ir) were prepared by dry impregnation of rutile ( $\text{TiO}_2$ -r, Aldrich, nanopowder, 99.5%), anatase ( $\text{TiO}_2$ -a, Aldrich, nanopowder, 99.7%), and  $\gamma\text{-Al}_2\text{O}_3$  (Alfa Aesar) with an aqueous solution of  $\text{IrCl}_3\text{-xH}_2\text{O}$  (ABCR, 99.9%) followed by drying at 393 K for 2 h and calcination as described above. Prior to the impregnation step, the carriers were calcined at 823 K for 5 h. Technical  $\text{IrO}_2$  catalysts were obtained by extrusion of the support materials followed by incorporation of the active phase by wet impregnation. First, water (0.45 cm<sup>3</sup> g<sup>-1</sup>) was added to pure  $\text{TiO}_2$ -r or  $\text{TiO}_2$ -a powder or to a mechanical mixture with 80 wt %  $\text{TiO}_2$ -r and 20 wt %  $\text{TiO}_2$ -a (denoted as  $\text{TiO}_2$ -ra) in a Caleva Mixer Torque Rheometer 3 to obtain a paste, which was then extruded into 2 mm diameter strands using a Caleva Mini Screw Extruder. The strands were cut into 4 mm long extrudates, which were dried at 333 K for 1 h and calcined at 823 K (for  $\text{TiO}_2$ -r and  $\text{TiO}_2$ -ra) or 1073 K (for  $\text{TiO}_2$ -a) in static air for 5 h using a heating rate of 5 K min<sup>-1</sup>. Wet impregnation of the shaped carriers was performed using an aqueous solution of  $\text{IrCl}_3\text{-xH}_2\text{O}$  (2 wt % Ir) for 20 h under ambient conditions. After removal of the excess water in a Büchi R-215 rotary evaporator at 308 K and 80 mbar, the obtained solids were freeze-dried at 190 K and 0.006 mbar for 24 h (Labconco FreeZone Plus 2.5 L) and then calcined at 823

K for 5 h. The labels of the shaped supports and catalysts contain the letter “e” for “extrudate”.

**2.2. Characterization.** The iridium content of the supported  $\text{IrO}_2$  catalysts prior to and after HCl oxidation was determined by wavelength-dispersive X-ray fluorescence (WDXRF) using a Bruker S4 Pioneer spectrometer. A 0.5 g sample was deposited into a polystyrene holder (34 mm diameter) and covered with a 4  $\mu\text{m}$  thick polypropylene foil. Standardless measurements were performed in He using the MultiRes-He34 acquisition program delivered with the SPECTRA Plus software from Bruker.  $\text{N}_2$  sorption at 77 K was measured using a Quantachrome Quadrasorb-SI gas adsorption analyzer. Prior to the measurement, the samples were degassed in vacuum at 473 K for 10 h. The Brunauer–Emmett–Teller (BET) method was applied to calculate the total surface area. Mercury porosimetry (MP) was carried out in a Micromeritics Autopore IV 9510 porosimeter. After the sample was degassed, mercury was intruded in the pressure range from vacuum to 418 MPa. The Washburn equation was applied to calculate the pore size distribution. Powder X-ray diffraction (XRD) data were measured using a PANalytical X’Pert PRO-MPD diffractometer. Data were recorded in the 10–70° 2 $\theta$  range with a step size of 0.017° and a counting time of 2.1 s per step. Temperature-programmed reduction with hydrogen (H<sub>2</sub>-TPR) was measured in a Thermo TPDRO 1100 unit. The samples were loaded in a quartz microreactor (11 mm i.d.), pretreated in He (20 cm<sup>3</sup> STP min<sup>-1</sup>) at 393 K for 60 min, and cooled to 323 K in He. The analysis was carried out in 5 vol % H<sub>2</sub>/N<sub>2</sub> (20 cm<sup>3</sup> STP min<sup>-1</sup>), ramping the temperature from 323 to 750 K at 2 K min<sup>-1</sup>. Thermogravimetric analysis (TGA) was performed using a Mettler Toledo TGA/DSC 1 Star system analyzer. Measurements were conducted in N<sub>2</sub> or air (40 cm<sup>3</sup> STP min<sup>-1</sup>), ramping the temperature from 298 to 1173 at 10 K min<sup>-1</sup>. X-ray photoelectron spectroscopy (XPS) experiments were carried out at the ISISS beamline of the BESSY II synchrotron facility of the Helmholtz Zentrum Berlin. Ir 4f and Cl 2p spectra were recorded under UHV with an electron kinetic energy of 700 eV. According to the TPP-2M formula of Tanuma, Powell, and Penn<sup>12</sup> for calculating inelastic mean free paths (IMFPs), the IMFP and information depth (3 × IMFP) are 11.0 and 33.0 Å, respectively, for 700 eV photoelectrons. Quantification was based on photoionization cross sections taken from Yeh and Lindau.<sup>13</sup> Digital reflected light microscopy images were obtained using a Leica DVM 5000 microscope equipped with a 2.11 megapixel charge-coupled device (CCD) camera and a tungsten halogen lamp. Scanning electron microscopy (SEM) was performed using a Zeiss Gemini 1530 FEG microscope operated at 5 kV after application of a thin platinum coating over the samples. High-resolution transmission electron microscopy (HRTEM) and high-resolution scanning transmission electron microscopy (HRSTEM) analyses were performed using an FEI Titan 80–300 microscope equipped with an image Cs corrector. The preparation of the samples comprised dry deposition of the powders on copper grids. Energy-filtered TEM (EFTEM) and electron energy loss spectroscopy (EELS) maps were acquired in the FEI microscope with a postcolumn Gatan Tridiem filter. For phase distribution analyses in the extrudates, ca. 80 nm thick cross sections were obtained by means of a microtome after the samples were embedded in a resin.<sup>14</sup> Elemental analysis and high-magnification high-angle annular dark-field (HAADF) STEM investigations were performed using an aberration-corrected Hitachi HD-2700CS microscope operated

at 200 kV and equipped with an energy-dispersive X-ray spectrometer (EDXS). The particle size distribution of the  $\text{TiO}_2$  powders was determined in an aqueous suspension by laser diffraction using a Malvern Mastersizer MS3000 instrument equipped with a wet dispersion unit and an ultrasonic device. The mechanical strength of the extrudates was assessed by a standardized crush test in a Tablet Tester 8 M (Dr. Schleuniger Pharmatron). The average crush strength was derived from measurements on 20 individual extrudates.

**2.3. Catalytic Tests.** The gas-phase oxidation of HCl was studied at ambient pressure in a setup described elsewhere.<sup>15</sup> The bulk and supported catalysts (0.4–0.6 mm particle size) were loaded in a continuous-flow fixed-bed quartz microreactor (8 mm i.d.) and pretreated in  $\text{N}_2$  (Pan Gas, purity 5.0) at 573 K for 30 min. Thereafter, a total volumetric flow ( $F_T$ ) of 166  $\text{cm}^3 \text{STP min}^{-1}$  containing 10 vol % HCl (Messer, purity 2.8, anhydrous) and 0–70 vol %  $\text{O}_2$  (Pan Gas, purity 5.0), balanced in  $\text{N}_2$ , was fed to the reactor at bed temperatures ( $T_{\text{bed}}$ ) in the range of 703–773 K. The steady-state activity during 5 h on stream at  $T_{\text{bed}} = 723$  K and a feed  $\text{O}_2/\text{HCl}$  ratio of 2 was measured using a catalyst weight ( $W_{\text{cat}}$ ) of 0.25 g, while the dependences of HCl conversion on temperature (at  $\text{O}_2/\text{HCl} = 2$ ) and on the feed  $\text{O}_2/\text{HCl}$  ratio (at  $T_{\text{bed}} = 723$  K) were determined using  $W_{\text{cat}} = 0.1$  g (0.25 g for supported catalysts). In the latter tests, data were collected after 1 h on stream under each set of conditions. Bulk catalysts ( $W_{\text{cat}} = 0.25$  g) were also tested at  $T_{\text{bed}} = 723$  K and  $\text{O}_2/\text{HCl} = 0$  (i.e., without  $\text{O}_2$  in the feed) for 5 h to evaluate their stability against chlorination and at  $T_{\text{bed}} = 823$  K and  $\text{O}_2/\text{HCl} = 0.5$  for 2 h to determine their robustness against overoxidation. The metal loss from the materials was derived from the difference in weight of the loaded reactors prior to and after testing. Catalysts in technical form, comprising extrudates with a diameter of 2 mm and a length of 4 mm were screened in a 17 mm i.d. quartz reactor using  $W_{\text{cat}} = 1.25$  g,  $F_T = 250 \text{ cm}^3 \text{STP min}^{-1}$ ,  $\text{O}_2/\text{HCl} = 2$ , and  $t = 1$  h. The most promising sample was assessed in kinetic tests using  $W_{\text{cat}} = 0.75$  g and  $F_T = 500 \text{ cm}^3 \text{STP min}^{-1}$  with varying temperature (703–773 K) and feed  $\text{O}_2/\text{HCl}$  ratio (0–7). A 50 h catalytic run was conducted with  $W_{\text{cat}} = 0.75$  g,  $F_T = 166 \text{ cm}^3 \text{STP min}^{-1}$ ,  $T_{\text{bed}} = 723$  K, and feed  $\text{O}_2/\text{HCl} = 2$ . The Carberry, Weisz–Prater, and non-isothermal transport criteria were fulfilled in all of our catalytic tests, indicating the absence of extra- and intraparticle mass and heat transfer limitations. Temperature gradients along the catalyst bed could not be experimentally assessed, but their presence cannot be excluded because of the exothermic nature of the reaction. Quantification of  $\text{Cl}_2$  at the reactor outlet was performed by iodometric titration in a Mettler Toledo G20 titrator. The percentage of HCl conversion was determined as  $X_{\text{HCl}} = (2 \times \text{moles of } \text{Cl}_2 \text{ at the reactor outlet}) / (\text{moles of HCl at the reactor inlet}) \times 100\%$ . The reaction rate was expressed as moles of  $\text{Cl}_2$  produced per minute per mol of Ir in the sample, and the space-time yield was determined as the mass of  $\text{Cl}_2$  produced per hour per gram of catalyst. The used catalysts were collected for ex situ characterization after the reactor was rapidly cooled to room temperature in a  $\text{N}_2$  flow.

### 3. COMPUTATIONAL DETAILS

Density functional theory (DFT) as implemented in the VASP code<sup>16,17</sup> was applied to slabs representing the (110) and (101) low-surface-energy facets of  $\text{IrO}_2$ . The exchange–correlation functional was RPBE.<sup>18</sup> The inner electrons were replaced by projected augmented wave (PAW) frozen core potentials,<sup>19</sup> and

monoelectronic valence states were expanded in plane waves with a cutoff energy of 450 eV. Each of the slabs contained five trilayers and a  $p(4 \times 1)$  reconstruction to investigate possible lateral interactions. The Monkhorst–Pack scheme was employed to generate the  $k$  points, which were  $2 \times 4 \times 1$  for the (110) surfaces.<sup>20</sup> Transition states were identified through the climbing image version of the nudged elastic band.<sup>21</sup> On the (110) and (101) surfaces, oxygen atoms show either threefold coordination (equivalent to the bulk,  $\text{O}_{3c}$ ) or twofold coordination (known as bridge oxygen atoms,  $\text{O}_b$ ). Coordinatively unsaturated Ir cations ( $\text{Ir}_{\text{cus}}$ ) with a coordination number of 5 are also present at the surface. To describe the different positions at the surfaces, we employed the subindex “b” if a given atom or fragment is adsorbed at a formerly  $\text{O}_b$  position and the subindex “cus” if it is adsorbed at a formerly open  $\text{Ir}_{\text{cus}}$  site. To represent the  $\text{RuO}_2/\text{TiO}_2$  catalyst, one [model  $\text{RuO}_2/\text{TiO}_2(1 \text{ ML})$ ] or two [model  $\text{RuO}_2/\text{TiO}_2(2 \text{ ML})$ ] epilayers of  $\text{RuO}_2$  were accommodated on top of  $\text{TiO}_2(110)$  (Figure S1 in the Supporting Information). The total thickness of these slabs corresponds to five layers, where the upper three layers were relaxed in all directions. The Wulff structure<sup>22</sup> of  $\text{IrO}_2$  presents about a 1:1 ratio of the (110) and (101) surfaces. The  $\text{TiO}_2$ -rutile employed as a support shows a different proportion, i.e., 84% corresponding to the (110) surface and the rest to the (101) surface.<sup>23</sup> In order to analyze the complete Deacon reaction on  $\text{IrO}_2$  nanoparticles, we considered the reaction paths on the two main  $\text{IrO}_2$  surfaces and on an  $\text{IrO}_2$  mono- and bilayer epitaxially grown over  $\text{TiO}_2$ .

## 4. RESULTS AND DISCUSSION

**4.1. Bulk  $\text{IrO}_2$ .** **4.1.1. Catalytic Performance.**  $\text{IrO}_2$  exhibited high and stable HCl conversion (~60%) over 5 h at 723 K and  $\text{O}_2/\text{HCl} = 2$  (Table 1). This activity level is similar to that

**Table 1. Characterization and Activity Data for  $\text{IrO}_2$  Catalysts**

sample	Ir (wt %) <sup>a</sup>		$S_{\text{BET}}$ ( $\text{m}^2 \text{ g}^{-1}$ )		$X_{\text{HCl}}$ (%) <sup>c</sup>	$E_{\text{a}}^{\text{app}}$ (kJ mol <sup>-1</sup> )
	fresh	after	fresh <sup>b</sup>	after		
$\text{IrO}_2$	85	—	8	8	63	82
$\text{IrO}_2/\text{TiO}_2$ <sup>r</sup>	2.0	2.0	24 (24)	23	28	58
$\text{IrO}_2/\text{TiO}_2$ <sup>a</sup>	2.0	2.0	48 (47)	37	5	78

<sup>a</sup>Determined by XRF. <sup>b</sup>Surface areas of the pure carriers are given in parentheses. <sup>c</sup>Conditions:  $W_{\text{cat}} = 0.25$  g,  $T_{\text{bed}} = 723$  K,  $\text{O}_2/\text{HCl} = 2$ ,  $F_T = 166 \text{ cm}^3 \text{STP min}^{-1}$ , and  $t = 5$  h.

exhibited by  $\text{RuO}_2$  at a ca. 170 K lower temperature (Figure 1a). As the difference in temperature (ca. 170 K) for the oxidative decomposition of  $\text{IrCl}_3$  and  $\text{RuCl}_3$  (Figure S2) is similar to that for their Deacon activity, the higher operating temperature required by  $\text{IrO}_2$  should be related to the more difficult evolution of chlorine. From the Arrhenius plot, the apparent activation energy for  $\text{IrO}_2$  was estimated at 82 kJ mol<sup>-1</sup> (Table 1 and Figure S3a). The HCl conversion over  $\text{IrO}_2$  decreased as the feed  $\text{O}_2/\text{HCl}$  ratio was lowered. The reaction order with respect to  $\text{O}_2$  was calculated to be 0.4, suggesting that catalyst reoxidation is the rate-determining step (Figure S3b), which is common to the majority of Deacon catalysts reported to date and indeed is tightly linked to chlorine desorption.<sup>8,15,23,24</sup> When an upward cycle going from more reducing to more oxidizing conditions (feed  $\text{O}_2/\text{HCl}$  from 0 to 7) was performed directly after the downward cycle, similar

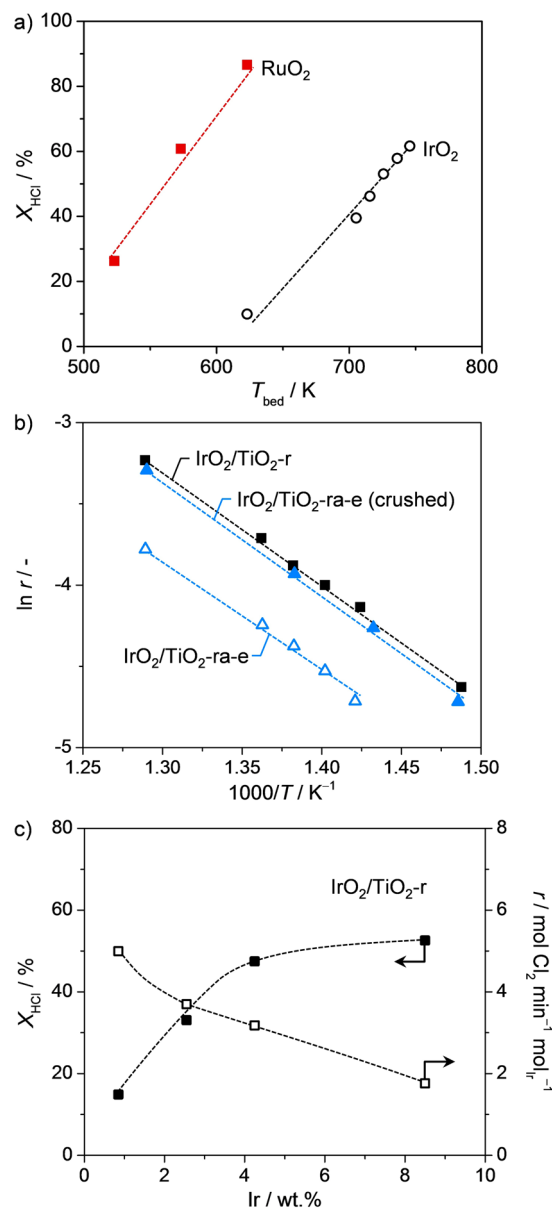


**Figure 1.** (a) HCl conversion vs bed temperature at  $O_2/HCl = 2$  over bulk  $\text{IrO}_2$  and  $\text{RuO}_2$ . (b) Arrhenius plots for  $\text{IrO}_2/\text{TiO}_2\text{-r}$ ,  $\text{IrO}_2/\text{TiO}_2\text{-ra-e}$ , and crushed  $\text{IrO}_2/\text{TiO}_2\text{-ra-e}$  at  $O_2/\text{HCl} = 2$ . (c) HCl conversion and Ir-specific reaction rate over  $\text{IrO}_2/\text{TiO}_2\text{-r}$  vs iridium loading at 723 K and  $O_2/\text{HCl} = 2$ .

HCl conversion levels were obtained (Figure S3b), indicating the remarkable stability of  $\text{IrO}_2$  under Deacon conditions. To further assess its resistance against chlorination,  $\text{IrO}_2$  was exposed to an HCl-only feed for 5 h at 723 K to produce samples for characterization. Moreover, in view of the exothermic character of the Deacon reaction, its robustness was also evaluated under harsher conditions where formation of the volatile  $\text{IrO}_3$  species may occur. At 823 K and  $O_2/\text{HCl} = 0.5$ ,  $\text{IrO}_2$  lost ca. 2.5% of its initial weight in the course of 2 h. Considering that the loss for  $\text{RuO}_2$  was 18% under the same conditions,  $\text{IrO}_2$  is more stable than  $\text{RuO}_2$  against oxidation.

**4.1.2. Characterization.** The surface area of  $\text{IrO}_2$  ( $S_{\text{BET}} = 8 \text{ m}^2 \text{ g}^{-1}$ ) remained unchanged after exposure to Deacon conditions (Table 1), which suggests resistance against sintering. This result contrasts with previous evidence for  $\text{RuO}_2$ .<sup>4</sup> The diffractogram of  $\text{IrO}_2$  after HCl oxidation coincides

with that of the fresh sample, showing only the characteristic reflections of iridium(IV) oxide (ICDD PDF-2 00-04301019), demonstrating that the catalyst did not undergo bulk chlorination (Figure 2a). A similar result was obtained for

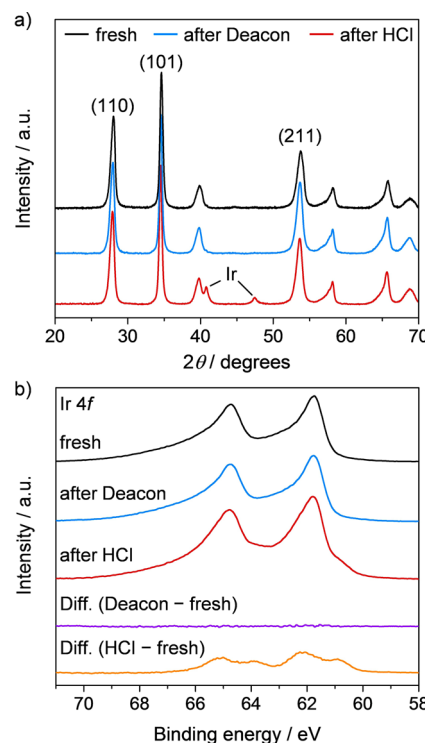


**Figure 2.** (a) XRD patterns and (b) Ir 4f core-level XPS spectra of bulk  $\text{IrO}_2$  in fresh form, after Deacon reaction at 723 K and  $O_2/\text{HCl} = 2$ , and after HCl treatment at 723 K. Unmarked reflections in (a) belong to the  $\text{IrO}_2$  phase.

$\text{RuO}_2$  upon testing under the same conditions (Figure S4a). Interestingly, a tiny amount of metallic iridium was detected in the XRD pattern of an  $\text{IrO}_2$  sample treated in HCl only. This might be explained by the formation of some chlorinated phases in the absence of gas-phase  $O_2$ , which produce Ir upon decomposition during the cooling of the sample in  $N_2$ . TGA analysis of  $\text{IrO}_2$  after HCl oxidation exhibited negligible weight loss with respect to the fresh material (Figure S4b), corroborating the absence of chlorinated phases, as for  $\text{RuO}_2$  (Figure S4c). Nonetheless, the sample treated in HCl-only produced a slightly more pronounced weight loss above 700 K, thus confirming a little degree of chlorination (Figure S4b). H<sub>2</sub>-TPR analysis of  $\text{IrO}_2$  in fresh form, after HCl oxidation (Deacon), and after HCl treatment produced comparable reduction profiles, supporting the absence of significant changes in particle size or chemical state by chlorination (Figure S5).

HRTEM of fresh  $\text{IrO}_2$  revealed the presence of big rodlike rutile crystals (Figure 3a). Exposure to Deacon conditions led to their partial transformation into nanosized crystallites (Figure 3b) while still preserving their rutile structure. In view of the  $N_2$  sorption and XRD results described above, the extent of this crystal modification is supposed to be moderate to minor. After HCl treatment, smaller particles were detected along with particles preserving their original dimensions. Crystals with sizes of 2 nm constitute the majority of these smaller particles, as after the Deacon reaction, but some crystals with sizes of ca. 10 nm are also present, whose nature is mostly

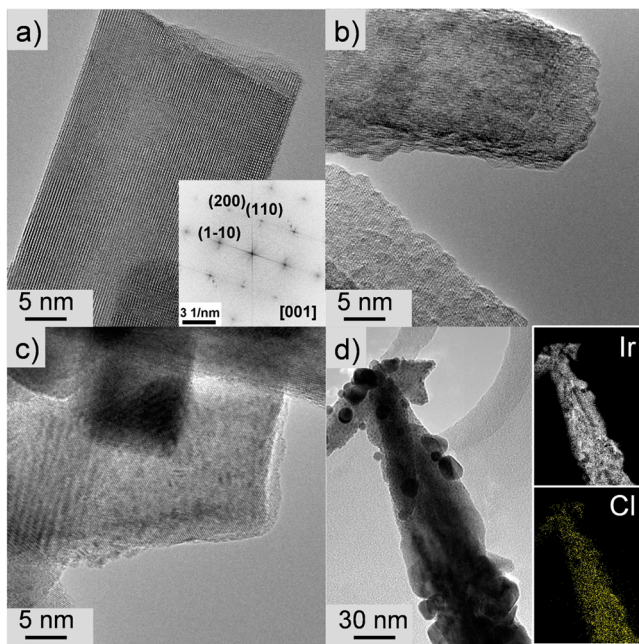


**Figure 3.** HRTEM of bulk  $\text{IrO}_2$  (a) in fresh form, (b) after Deacon reaction, and (c, d) after HCl treatment. The inset in (a) displays the electron diffraction pattern of  $\text{IrO}_2$ , while those in (d) show the EELSM mappings of Ir and Cl.

metallic according to HRTEM analysis. The latter correspond to the metallic Ir phase evidenced by XRD. A distinct  $\text{IrCl}_3$  phase was not detected, but EFTEM maps suggested the presence of Cl on the surface of the  $\text{IrO}_2$  particles (Figure 3c,d).

XPS analyses were performed to characterize the surface chlorination of  $\text{IrO}_2$  after Deacon and HCl treatment. The corresponding Ir 4f spectra of fresh and used samples are depicted in Figure 2b. Ir 4f appears as a doublet (as all of the core levels except for the s states), whose shape is strongly asymmetric in all of the cases. This is due to the high density of states at the Fermi level and the high degree of core hole screening.<sup>25</sup> The observed binding energy of 61.8 eV ( $7/2$ ) for the fresh sample fits well to an earlier report on  $\text{IrO}_2$ .<sup>26</sup> The Ir 4f spectrum did not change upon HCl oxidation (the difference spectrum is a flat line), and thus, no new surface phases arose as a result of the catalytic process. In contrast, after HCl treatment, two new doublets appeared (see the difference spectrum). The low-binding-energy component (~60.9 eV) is associated with metallic Ir, which has an asymmetric line shape. The higher-binding-energy component (62.2–62.3 eV) is not asymmetric and is assigned to  $\text{IrCl}_3$ , in reasonable agreement with the literature value (62.7 eV).<sup>27</sup> Concerning the Cl content, the fresh sample already contained some Cl (Cl/Ir = 0.18), suggesting that not all of the Cl was removed during calcination. Nevertheless, its amount was small since it did not influence the Ir 4f spectrum. Surface chlorination occurred upon HCl oxidation under the examined conditions (Cl/Ir = 0.47). However, neither subsurface chlorination nor bulk chloride phase formation was found. The Cl 2p spectra of the samples (Figure S6) contain at least three components, probably related to Cl sitting on  $\text{Ir}_{\text{cus}}$  sites and bridge sites and some more oxidized Cl species.<sup>28</sup> After HCl treatment, the chlorine content further increased (Cl/Ir = 0.8), in line with the formation of  $\text{IrCl}_3$ . The  $\text{IrCl}_3$  signal in Cl 2p probably strongly

overlaps with that of bridge Cl, disabling differentiation of these species (Figure S6).

**4.1.3. Molecular Modeling.** HCl oxidation on  $\text{IrO}_2$  takes place following the mechanism described previously by some of us and others,<sup>4,10,28</sup> which comprises the following steps:

Oxygen adsorption with subsequent dissociation:



HCl adsorption by proton stripping:



Recombination of hydroxyls on the surface:



Water desorption:



Chlorine desorption:



The corresponding reaction profile is shown in Figure 4. Both the adsorption of oxygen and chlorine over  $\text{IrO}_2$  turned out to

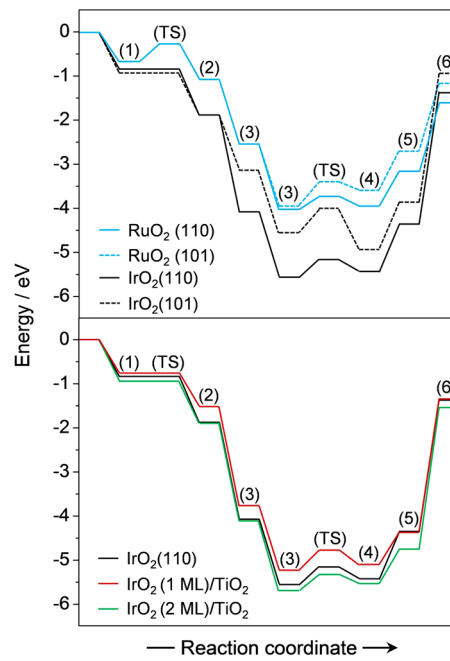


**Figure 4.** Reaction profile of HCl oxidation on different (top) bulk catalysts and (bottom) supported  $\text{IrO}_2$  model catalysts. The numbering follows the final states in eqs 1–6. For instance, “(1)” is adsorbed molecular  $\text{O}_2$  and “(2)” stands for the dissociated state. The transition states for  $\text{O}_2$  dissociation between (1) and (2) and OH recombination to give water (S) are marked as “(TS)”. It should be noted that as the profile corresponds to half a stoichiometric reaction ( $\text{O}_2 + 2\text{HCl} \rightarrow \text{O}^* + \text{H}_2\text{O} + \text{Cl}_2$ ), step (3) occurs twice and in the final state an oxygen atom is left on the surface.

be much more exothermic than over  $\text{RuO}_2$ . This has two important consequences: (i) no barrier is observed for the dissociation of oxygen on the surface and (ii) the energy required for chlorine evolution to the gas phase is very high. As for  $\text{RuO}_2$ ,<sup>4</sup> lateral interactions reduce the chlorine desorption barrier to a certain extent. This was confirmed for  $\text{IrO}_2$  by

performing calculations with a large  $p(4 \times 1)$  supercell at full Cl coverage, which indicated that the energy associated with this step is reduced by 0.4 eV. Still, the barrier is far too large to enable chlorine evolution under the conditions where  $\text{RuO}_2$  is active. This explains the higher operating temperature required by  $\text{IrO}_2$ . These results are in good correspondence with those obtained by Studt et al.<sup>10,29</sup>

Oxidation leading to the formation of volatile species and bulk chlorination have been mentioned above as collateral processes during HCl oxidation. For  $\text{RuO}_2$ , the former is known to happen by the following reaction:

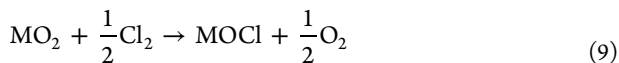


According to the calculations, the oxidation is mildly endothermic (0.83 eV). Experimentally,  $\text{RuO}_4$  is volatile at 673 K (vide supra). The  $\text{IrO}_2$  case is somewhat different, as  $\text{IrO}_3$  is formed instead:



There is a clear indication in the literature that the formation of  $\text{IrO}_3$  is less likely than that of  $\text{RuO}_4$ ,<sup>30</sup> explaining the higher stability of  $\text{IrO}_2$  against oxidation under the conditions applied in the experiments.

With regard to bulk chlorination, two different analyses were performed to assess the penetration of chlorine into the lattice and to account for the Cl coverage. The former was based on the replacement energy calculated according to the reaction:



where M = Ir or Ru and the Cl atom either replaces a bridge position on the (110) facet or a bulk O atom in the lattice. The corresponding plot is presented in Figure S7a. While the energy demand for bridge substitution is minor and similar for both oxides, incorporation in the plane induces a large distortion that requires about 1.7 eV for  $\text{RuO}_2$  and 2 eV for  $\text{IrO}_2$ . Therefore, an even slightly higher robustness against bulk chlorination is found for  $\text{IrO}_2$ .

Concerning the Cl coverage, we analyzed the different configurations that might appear on the surface by allowing both bridge and cus positions to be occupied by O or Cl and then determining the energies for a  $p(2 \times 1)$  supercell using a methodology previously formulated for  $\text{RuO}_2$ .<sup>3</sup> The energies corresponding to the different configurations are presented in Figure S7b. The larger binding energies found for both O and Cl in the case of  $\text{IrO}_2$  compared with  $\text{RuO}_2$  clearly relate to the large stabilization obtained for densely populated surfaces. The average coverage at the same temperature should be higher for  $\text{IrO}_2$  than for  $\text{RuO}_2$ , although it is already very high for  $\text{RuO}_2$ , as shown in our previous experiments and microkinetic modeling.<sup>24</sup> Further inspection of the diagrams indicates that a configuration with all of the cus positions occupied and about 50% of the  $\text{O}_b$  sites replaced by Cl would be most likely under the experimental reaction conditions for  $\text{IrO}_2$ .

**4.2. Supported  $\text{IrO}_2$  Catalysts.** **4.2.1. Catalytic Performance.** On the basis of the outstanding performance and robustness of bulk  $\text{IrO}_2$  in HCl oxidation, we focused on optimizing its utilization by deposition onto a suitable carrier.  $\text{TiO}_2$ -rutile was selected in view of the expected positive influence of the structural and lattice matching with the active phase.<sup>5,31</sup> The anatase polymorph was used for comparative purposes. Supported catalysts (2 wt % Ir) were prepared by dry

impregnation and tested in HCl oxidation at  $\text{O}_2/\text{HCl} = 2$  and 723 K for 5 h on stream (Table 1). The HCl conversion over  $\text{IrO}_2/\text{TiO}_2\text{-r}$  was stable and 6 times higher than that over  $\text{IrO}_2/\text{TiO}_2\text{-a}$  (28% vs 5%, respectively). Normalization of the chlorine production rates over these catalysts to the total amount of iridium clearly shows that the metal is best utilized in the  $\text{TiO}_2\text{-r}$ -supported material (Figure S3c). The apparent activation energy over  $\text{IrO}_2/\text{TiO}_2\text{-r}$  was estimated to be only 58 kJ mol<sup>-1</sup> (Figure 1b), while that of  $\text{IrO}_2/\text{TiO}_2\text{-a}$  was 78 kJ mol<sup>-1</sup> (Figure S3a), which is comparable to the value determined on bulk  $\text{IrO}_2$  (Table 1). The reaction order in  $\text{O}_2$  over  $\text{IrO}_2/\text{TiO}_2\text{-r}$  was 0.5 (Figure S3b), which is also similar to that obtained over bulk  $\text{IrO}_2$ . These results extend the remarkable effect of the  $\text{TiO}_2\text{-r}$  carrier also to other rutile-type active phases besides  $\text{RuO}_2$ . This is further substantiated by the poor activity (HCl conversion = 8%) of an  $\text{IrO}_2$  catalyst prepared in an identical manner using another structurally different support such as  $\gamma\text{-Al}_2\text{O}_3$ .

In view of a possible technical application, the metal content in the catalyst should be kept as low as possible to minimize its cost, particularly in the case of expensive metals such as iridium. Thus,  $\text{IrO}_2/\text{TiO}_2\text{-r}$  catalysts with a nominal Ir loading between 1 and 10 wt % were prepared and tested. Figure 1c shows the HCl conversion and  $\text{Cl}_2$  production rates per mole of iridium as a function of the loading. The HCl conversion increased with the iridium content, while the Ir-specific reaction rate decreased. A compromise between activity and Ir-specific  $\text{Cl}_2$  production was identified between 2 and 4 wt % Ir.

**4.2.2. Characterization.** Both the  $\text{TiO}_2\text{-r}$  and  $\text{TiO}_2\text{-a}$ -supported catalysts contained 2.0 wt % Ir, as determined by XRF (Table 1). The metal content was unaltered after 5 h on stream, underlining the stability of  $\text{IrO}_2$  against oxidation and volatilization. The surface area of  $\text{IrO}_2/\text{TiO}_2\text{-a}$  was almost twice as large as that for  $\text{IrO}_2/\text{TiO}_2\text{-r}$  (Table 1). After reaction, the  $S_{\text{BET}}$  of  $\text{IrO}_2/\text{TiO}_2\text{-r}$  was unaltered, while a moderate loss in surface area was found for  $\text{IrO}_2/\text{TiO}_2\text{-a}$  that could be related to sintering. As the HCl conversion over  $\text{IrO}_2/\text{TiO}_2\text{-a}$  was constant during the 5 h test, the catalyst modification should have occurred within the first few minutes on stream. The diffractogram of fresh  $\text{IrO}_2/\text{TiO}_2\text{-a}$  evidences the presence of the  $\text{IrO}_2$  phase (ICDD PDF-2 00-04301019) in addition to that for titania-anatase (ICDD PDF-2 01-071-1168), which points to the presence of rather large  $\text{IrO}_2$  aggregates on this carrier (Figure 5a). In contrast, the XRD pattern of  $\text{IrO}_2/\text{TiO}_2\text{-r}$  exhibits only the reflections of titania-rutile (ICDD PDF-2 01-076-0325), pointing to the existence of very small  $\text{IrO}_2$  nanostructures. XRD analysis of the used catalysts did not indicate major variations for the active and support phases or the formation of chlorinated species. The fresh catalysts were further analyzed by  $\text{H}_2\text{-TPR}$  (Figure 5b). For  $\text{IrO}_2/\text{TiO}_2\text{-a}$ , a single reduction peak was observed between 475 and 575 K with a maximum at 500 K, pointing toward the presence of particles with a rather homogeneous size distribution. In contrast, the reduction profile of  $\text{IrO}_2/\text{TiO}_2\text{-r}$  shows a distinct peak at 397 K and a broad reduction signal with a maximum at 606 K and a shoulder at 570 K (Figure 5b). The low-temperature peak likely refers to highly dispersed  $\text{IrO}_2$ , while the complex, high-temperature signal may indicate the presence of  $\text{IrO}_2$  species that more strongly interact with the  $\text{TiO}_2\text{-r}$  support, possibly as a result of the lattice matching, as already observed for  $\text{RuO}_2$  on  $\text{TiO}_2\text{-r}$ .<sup>31,32</sup> Overall, these characterization results suggest differences in morphology and dispersion of the  $\text{IrO}_2$  phase induced by the support characteristics. Thus,

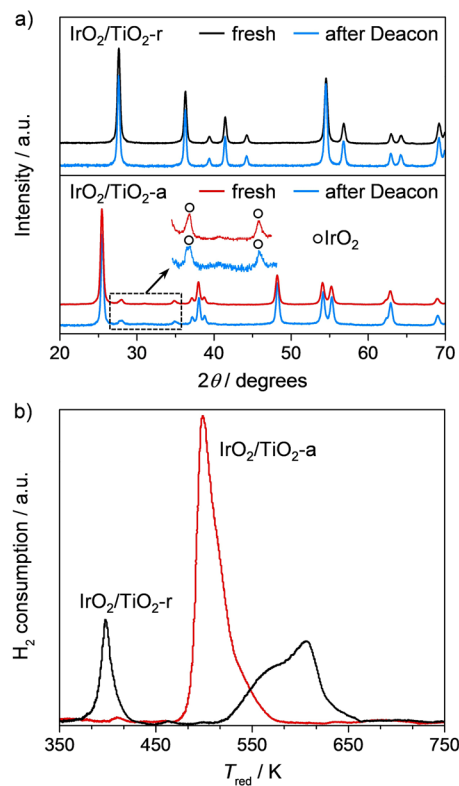


**Figure 5.** (a) XRD patterns of  $\text{IrO}_2/\text{TiO}_2\text{-r}$  and  $\text{IrO}_2/\text{TiO}_2\text{-a}$  in fresh form and after Deacon reaction at 723 K and  $\text{O}_2/\text{HCl} = 2$ . Unmarked reflections belong to the rutile and anatase carriers. (b)  $\text{H}_2$ -TPR profiles of  $\text{IrO}_2/\text{TiO}_2\text{-r}$  and  $\text{IrO}_2/\text{TiO}_2\text{-a}$  in fresh form.

the catalysts were further investigated by means of electron microscopy techniques.

As  $\text{IrO}_2$  and  $\text{TiO}_2\text{-r}$  cannot be distinguished by HRTEM because of their identical crystalline structures and similar unit cells, HRSTEM was applied to identify different phases arising from the variation in  $Z$  contrast. Accordingly, atomically dispersed  $\text{IrO}_2$  clusters were visualized to decorate the  $\text{TiO}_2\text{-r}$  particles (Figure 6a). After reaction, the clusterlike distribution of  $\text{IrO}_2$  on  $\text{TiO}_2\text{-r}$  was preserved, but fewer clusters were identified (Figure 6b). Since the Ir content in the catalysts was unchanged (vide supra), a certain degree of agglomeration of the clusters could be likely, although no defined  $\text{IrO}_2$  particles could be identified. HRTEM analysis of the fresh  $\text{TiO}_2\text{-a}$ -supported samples revealed the presence of crystalline  $\text{IrO}_2$  nanoparticles (Figure 6c,d), which underwent partial roughening during the  $\text{HCl}$  oxidation (Figure 6d). These results strongly point to an enhanced dispersion as the main reason for the higher activity of  $\text{IrO}_2/\text{TiO}_2\text{-r}$ , in line with the improved metal utilization highlighted above (Figure S3c). Nonetheless, because of the cluster-like structure of the active phase in  $\text{IrO}_2/\text{TiO}_2\text{-r}$ , additional favorable effects of an electronic nature exclusive of the titania-rutile support cannot be ruled out. Such effects have recently been uncovered for small, thin, and well-dispersed  $\text{RuO}_2$  particles on  $\text{TiO}_2\text{-r}$ .<sup>31</sup> The lower activation energy for the rutile-supported system compared with the anatase-supported system (vide supra) could also relate to a modification of the electronic properties that might influence the binding energies of the reactants and products and therefore the energetics of the rate-limiting step.

**4.2.3. Molecular Modeling.** The support effect was further investigated theoretically with respect to both geometric and

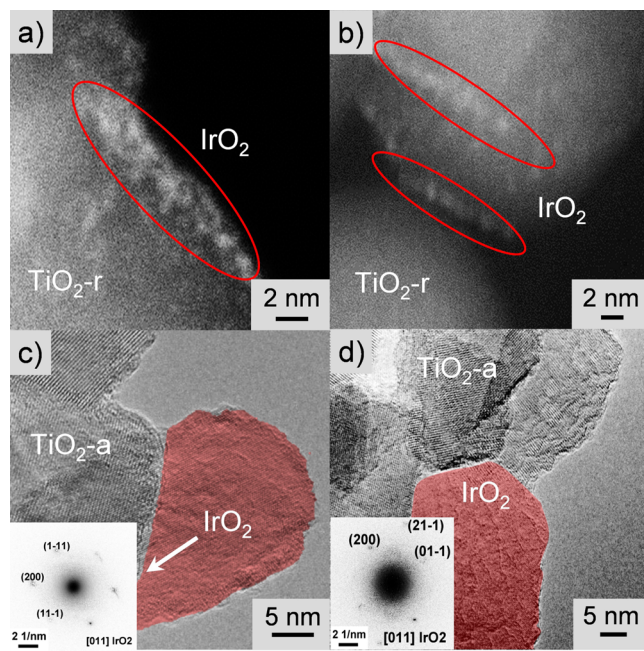


**Figure 6.** (a, b) HRSTEM of  $\text{IrO}_2/\text{TiO}_2\text{-r}$  and (c, d) HRTEM of  $\text{IrO}_2/\text{TiO}_2\text{-a}$  in (a, c) fresh form and (b, d) after Deacon reaction. The red ovals in (a) and (b) encircle  $\text{IrO}_2$  clusters, while  $\text{IrO}_2$  particles in (c) and (d) are highlighted by red contrast. The insets in (c) and (d) show the electron diffraction patterns of  $\text{IrO}_2$ .

electronic aspects. In the case of anatase,  $\text{IrO}_2$  overlayers are clearly not stable, and the active phase should be in the form of particles. For rutile, the growth of  $\text{IrO}_2$  epilayers implies a geometric distortion of  $-7$  and  $-2\%$  in the surface planes of the (110) surface. This strain might lead to Stranski-Krastanov growth. Accordingly, the first (or few)  $\text{IrO}_2$  layers would be in registry with the support and the rest would build up tridimensional oxide islands, in agreement with the electron microscopy results. The islands would behave similarly to bulk  $\text{IrO}_2$ , while the activity of the epitaxial overlayers would be affected by the presence of the support. Oxygen and chlorine adsorption are indeed modified with respect to the native material, as clearly seen in the reaction profiles (Figure 4). For a single monolayer, mainly electronic contributions arise. As a result, the binding energy of oxygen is reduced by about 0.1 eV and that of Cl remains almost constant. As  $\text{IrO}_2$ -based catalysts are severely poisoned by Cl adsorption, the decrease in oxygen binding energy will not have a positive effect on the activity. Similar results were found for a single monolayer of  $\text{RuO}_2$  on  $\text{SnO}_2$ , which was predicted to be less active than bulk  $\text{RuO}_2$ ,<sup>24</sup> or on  $\text{TiO}_2\text{-r}$ , for which higher binding energies have also been retrieved.<sup>33</sup> For two monolayers, as a result of geometric constrictions induced by the support, the adsorption energies of both O and Cl are larger than for bulk  $\text{IrO}_2$ , leading to less active catalysts. Therefore, the activity largely originates from the  $\text{IrO}_2$  islands on top of the possibly formed epilayers. The material gap between the perfect lattice and the modified lattice introduced by the clustering of the active phase on  $\text{TiO}_2\text{-r}$  should explain the modification in electronic properties and the lowering of the apparent activation energy over this catalyst.

**4.3. Scale-Up in Technical Form.** **4.3.1. Design of a Technical Catalyst.** Hereon, we demonstrate a rational pathway for the design of a technical  $\text{TiO}_2\text{-r}$ -supported  $\text{IrO}_2$  catalyst based on the preparation of a suitably shaped carrier

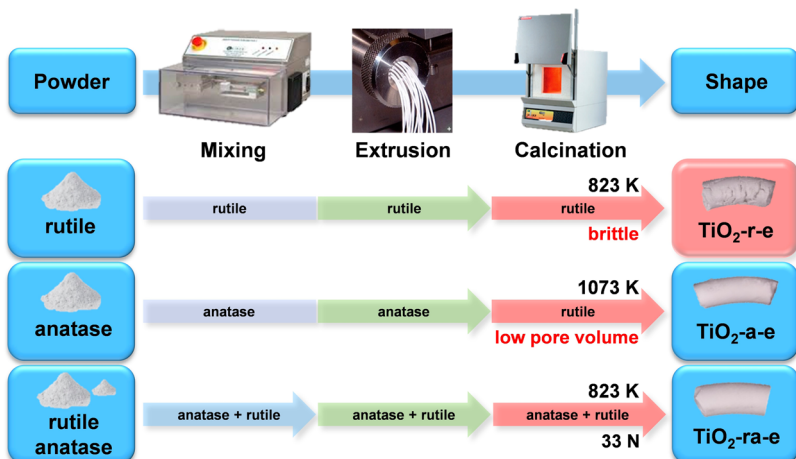


**Figure 7.** Preparation routes for technical carriers by extrusion and calcination from pure  $\text{TiO}_2$ -r ( $\text{TiO}_2$ -r-e),  $\text{TiO}_2$ -a ( $\text{TiO}_2$ -a-e), or a mechanical mixture of 80 wt %  $\text{TiO}_2$ -r and 20 wt %  $\text{TiO}_2$ -a ( $\text{TiO}_2$ -ra-e). The obtained extrudates (right) were visualized by optical microscopy.

followed by deposition of the active phase. Three protocols were followed, as schematically summarized in Figure 7. At first, we attempted to directly extrude  $\text{TiO}_2$ -r. As its particle size distribution is very homogeneous and the particles are smaller than 50  $\mu\text{m}$  (Figure 8a), no pretreatment (e.g., wet milling) of

the powder was undertaken. Analysis of the produced  $\text{TiO}_2$ -r-e by optical microscopy evidenced many radial cracks (Figure 7), indicating that rutile possesses insufficient self-binding properties. Ultrasonication of the nanopowder in the particle analyzer indeed led to breakage of the particles into several smaller fractions with sizes of 0.15–20  $\mu\text{m}$ , indicating weak interparticle forces. SEM images of the extrudates also highlighted that  $\text{TiO}_2$ -rutile agglomerates are made of large particles organized in clusters that are separated by substantial voids, which strongly reduce the contact area between the clusters (Figure S8a).

An often-reported strategy to aid the shaping process of  $\text{TiO}_2$  is the facilitative addition of organics to the powder.<sup>34,35</sup> However, the subsequent removal of the organics from the shaped bodies may impose difficulties and ultimately affect the catalyst properties. Thus, our attention was directed toward inorganic extrusion aids, and  $\text{TiO}_2$ -a seemed suitable to the purpose. In contrast to  $\text{TiO}_2$ -r, its particle size distribution did not change upon ultrasonication, suggesting rather strong interparticle forces. Furthermore, its larger surface area (Table 1) and its dense particle packing, as visualized by SEM (Figure S8b), should favor the formation of liquid bridges between the particles and thus improve the extrusion quality.<sup>36</sup> Besides its use as additive, since  $\text{TiO}_2$ -a can be transformed into the rutile polymorph, we also conceived a procedure involving extrusion of  $\text{TiO}_2$ -a only and exposure of the shaped bodies to a temperature treatment to induce the phase change. Thus, extrudates were generated by adding 20 wt %  $\text{TiO}_2$ -a as shaping aid in a mechanical mixture with the main  $\text{TiO}_2$ -r phase ( $\text{TiO}_2$ -ra-e) as well as by shaping pure  $\text{TiO}_2$ -a and applying a calcination step at 1073 K ( $\text{TiO}_2$ -a-e). The so-prepared bodies did not exhibit any cracks or other optically detectable defects (Figure 7). XRD analysis confirmed the coexistence of the  $\text{TiO}_2$ -a and  $\text{TiO}_2$ -r phases in  $\text{TiO}_2$ -ra-e in the expected proportion and the complete phase transformation from anatase to rutile for  $\text{TiO}_2$ -a-e (Figure S9a). The mechanical side-crush strengths for both types of extrudates were high enough to ensure sufficient mechanical stability (Table 2). With respect to the textural properties, while the surface area of  $\text{TiO}_2$ -a-e drastically dropped because of sintering, the original  $S_{\text{BET}}$  of the powder was retained in  $\text{TiO}_2$ -ra-e (Table 2). Furthermore, the pore size distribution of  $\text{TiO}_2$ -r was preserved in  $\text{TiO}_2$ -ra-e, although the pore volume determined by mercury

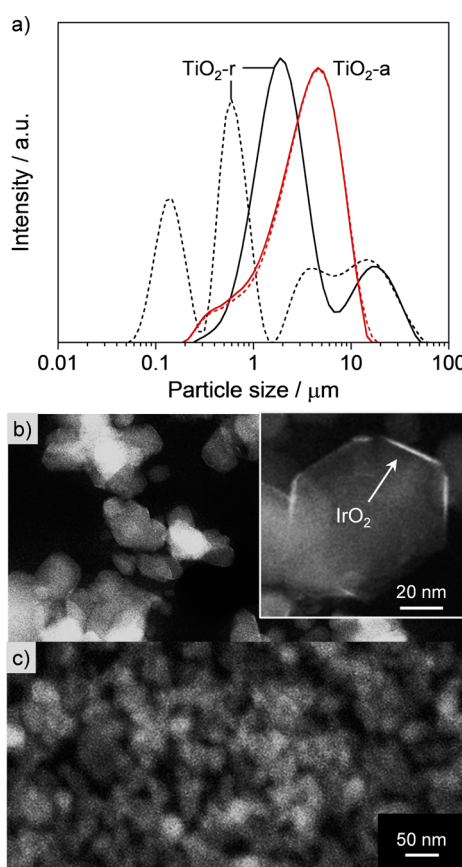


**Figure 8.** (a) Particle size analysis of the  $\text{TiO}_2$ -a and  $\text{TiO}_2$ -r carriers. Solid lines correspond to as-received oxides in suspension and dashed lines to materials after ultrasonication for 1 min. (b, c) HAADF-STEM images of a microtome-cut cross section of an  $\text{IrO}_2$ / $\text{TiO}_2$ -ra-e extrudate showing (b)  $\text{TiO}_2$ -r-rich and (c)  $\text{TiO}_2$ -a-rich zones. The inset in (b) depicts a section of a  $\text{TiO}_2$ -r crystal supporting  $\text{IrO}_2$ , which is visible along the edges of the carrier grain.

**Table 2. Characterization and Activity Data for the  $\text{IrO}_2$  Catalysts in Extrudate Form**

sample	Ir (wt %) <sup>a</sup>	side-crush strength (N) <sup>b</sup>	$S_{\text{BET}}$ ( $\text{m}^2 \text{g}^{-1}$ ) <sup>c</sup>	$V_{\text{pore}}$ ( $\text{cm}^3 \text{g}^{-1}$ )	$X_{\text{HCl}}$ (%) <sup>d</sup>
$\text{IrO}_2/\text{TiO}_2\text{-ra-e}$	2.1	33	25 (28)	0.36	43
$\text{IrO}_2/\text{TiO}_2\text{-a-e}$	2.1	120	1 (3)	0.12	18

<sup>a</sup>Determined by XRF. <sup>b</sup>Identical to the corresponding technical carriers. <sup>c</sup>Surface areas of the shaped carriers are given in parentheses. <sup>d</sup>Conditions:  $W_{\text{cat}} = 1.25 \text{ g}$ ,  $T_{\text{bed}} = 723 \text{ K}$ ,  $\text{O}_2/\text{HCl} = 2$ ,  $F_{\text{T}} = 250 \text{ cm}^3 \text{ STP min}^{-1}$ , and  $t = 1 \text{ h}$ .

intrusion decreased (Figure S9b), whereas  $\text{TiO}_2\text{-a-e}$  featured almost no porous structure and less pore volume than  $\text{TiO}_2\text{-ra-e}$  (Table 2). SEM imaging evidenced the presence of large rutile particles with diameters of 200 nm, confirming sintering during the preparation of  $\text{TiO}_2\text{-a-e}$  (Figure S8c). This was also clearly detected at a macroscopic level by the noticeable decrease in the diameter of the extrudates (Figure S10). For  $\text{TiO}_2\text{-ra-e}$ , small anatase particles were observed to fill the voids between  $\text{TiO}_2\text{-r}$  clusters of substantially smaller size (Figure S8d).

Two technical catalysts were prepared by wet impregnation with a loading of 2.0 wt % Ir on  $\text{TiO}_2\text{-ra-e}$  and  $\text{TiO}_2\text{-a-e}$  (Table 2). On the basis of optical microscopy imaging, the  $\text{IrO}_2$  phase appeared to be distributed uniformly in  $\text{TiO}_2\text{-ra-e}$ , almost reaching the core of the extrudates (Figure S10a). In contrast,  $\text{IrO}_2$  deposited exclusively at the external surface of  $\text{TiO}_2\text{-a-e}$  in a kind of eggshell configuration (Figure S10b). This disadvantageous result is related to the poor textural properties of the shaped carrier.

**4.3.2. Catalytic Performance and Characterization.** Testing of the two materials in HCl oxidation indicated that  $\text{IrO}_2/\text{TiO}_2\text{-ra-e}$  is 2.5 times more active than  $\text{IrO}_2/\text{TiO}_2\text{-a-e}$  (Table 2). As HCl oxidation is not diffusion limited, it is expected that a better metal distribution and utilization is achieved with a close to uniform rather than an eggshell-type configuration. Analysis of a microtome-cut cross section of an  $\text{IrO}_2/\text{TiO}_2\text{-ra-e}$  extrudate by electron microscopy techniques showed that  $\text{IrO}_2$  was preferentially deposited on  $\text{TiO}_2\text{-r}$ . In regions rich in rutile particles,  $\text{IrO}_2$  was indeed detected along the edges of the  $\text{TiO}_2\text{-r}$  particles (Figure 8b), while no  $\text{IrO}_2$  was found in sections with mainly  $\text{TiO}_2\text{-a}$  (Figure 8c). This is most likely due to the dense packing of the anatase phase, which might have hampered the impregnation of its surface (Figure S8b). Furthermore, it cannot be discarded that Ir species initially deposited on anatase migrated to the rutile phase during calcination. This process could be facilitated by lattice matching of  $\text{IrO}_2$  on  $\text{TiO}_2\text{-r}$ , which is in line with previous evidence for  $\text{RuO}_2/\text{SnO}_2\text{-Al}_2\text{O}_3$ .<sup>7</sup>

Kinetic tests on  $\text{IrO}_2/\text{TiO}_2\text{-ra-e}$  indicated that the activation energy (Figure 1b) and reaction order in  $\text{O}_2$  (Figure S3b) were similar to those for  $\text{IrO}_2/\text{TiO}_2\text{-r}$ , evidencing that the apparent kinetic behavior of supported  $\text{IrO}_2$  was preserved upon scale-up. These results further support the conclusion that no significant internal diffusion limitation exists within the technical catalyst. In order to compare the performance of the technical and supported materials under identical reaction conditions, a sample was prepared by crushing  $\text{IrO}_2/\text{TiO}_2\text{-ra-e}$ . The chlorine production rates were similar (Figure 1b), indicating no detrimental effect due to the presence of anatase and supporting the preferential deposition of  $\text{IrO}_2$  on rutile. The  $\text{IrO}_2/\text{TiO}_2\text{-ra-e}$  catalyst was subjected to a 50 h catalytic

run to assess its stability in a more extended time frame (Figure 9). The HCl conversion level (ca. 28%) dropped only slightly

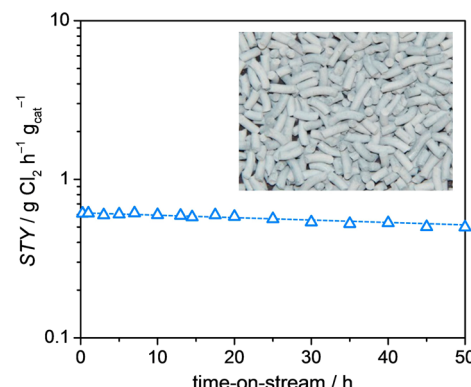


**Figure 9.** Space-time yield (STY) vs time on stream over  $\text{IrO}_2/\text{TiO}_2\text{-ra-e}$ . The inset shows a photograph of the extrudates.

during the test. Thus, the  $\text{IrO}_2/\text{TiO}_2\text{-ra-e}$  catalyst appears to be robust enough for further consideration as a high-temperature Deacon catalyst. The activity loss might relate to agglomeration of the supported  $\text{IrO}_2$  clusters, as hinted in section 4.2.2. To minimize this phenomenon in long-term use, the incorporation of additives (e.g.,  $\text{SiO}_2$  or  $\text{Al}_2\text{O}_3$ ) would be expected to be effective in stabilizing the active phase, in similarity with  $\text{RuO}_2$ -based industrial catalysts.<sup>5</sup>

In view of a technical application, it is worth noting that the price of iridium has reached new record levels in the past 2 years, making it significantly more expensive than ruthenium and thus rendering the implementation of an Ir-based industrial process unattractive at present (Figure S11). However, the prices of iridium and ruthenium are very volatile and independent from each other, so no speculations can be put forward for the near future. Indeed, it already happened in 2007–2008 that iridium was remarkably cheaper than ruthenium.

## 5. CONCLUSIONS

This study has confirmed the potential of  $\text{IrO}_2$  as a suitable catalyst for chlorine recycling via HCl oxidation, complementing the currently applied  $\text{RuO}_2$ -based systems. Activity and stability evaluation on bulk  $\text{IrO}_2$ , combined with in-depth characterization and DFT modeling, demonstrated that this material is active at a ca. 170 K higher temperature than  $\text{RuO}_2$  and that its stability is outstanding with respect to both chlorination and oxidation to volatile species. The higher operating temperature of  $\text{IrO}_2$  is due to the higher computed energy barrier for chlorine evolution in comparison with  $\text{RuO}_2$ .  $\text{TiO}_2$ -rutile was identified as a superior carrier for  $\text{IrO}_2$ , verifying the importance of the lattice matching between the active phase and the support to guarantee outstanding metal dispersion. Interestingly, the thin layer structure typical of  $\text{RuO}_2$  supported on rutile carriers was not observed here, as  $\text{IrO}_2$  rather formed well-distributed clusters. Using  $\text{TiO}_2$ -anatase as an extrusion aid enabled the manufacture of a mechanically stable technical  $\text{IrO}_2/\text{TiO}_2$ -rutile catalyst in extrudate form. The technical catalyst exhibits a high and stable space-time yield, making feasible its industrial utilization. This will be tightly related to the price evolution of noble metals.

## ■ ASSOCIATED CONTENT

### ■ Supporting Information

Models of  $\text{IrO}_2$  on  $\text{TiO}_2$ ; TGA of  $\text{IrCl}_3$  and  $\text{RuCl}_3$ ; kinetic data of  $\text{RuO}_2$  and  $\text{IrO}_2$ -based catalysts; XRD, TGA,  $\text{H}_2$ -TPR, and XPS analyses of the bulk catalysts; chlorine penetration profiles and energy configurations for bulk  $\text{IrO}_2$  and  $\text{RuO}_2$ ; SEM images of the  $\text{TiO}_2$  supports; XRD and mercury porosimetry of the technical carriers; optical microscopy images of the technical catalysts; and comparative price evolution of iridium and ruthenium. This material is available free of charge via the Internet at <http://pubs.acs.org>.

## ■ AUTHOR INFORMATION

### Corresponding Author

\*Fax: +41 44 633 1405. E-mail: jpr@chem.ethz.ch.

### Notes

The authors declare no competing financial interest.

## ■ ACKNOWLEDGMENTS

We thank Bayer MaterialScience for permission to publish these results and the Electron Microscopy Centre of the Swiss Federal Institute of Technology (EMEZ) for use of their facilities. Dr. Sharon Mitchell is acknowledged for microscopy investigation. N.L. is indebted to MINECO (CTQ2012-33826) and BSC-RES for providing generous computational resources.

## ■ REFERENCES

- (1) Pérez-Ramírez, J.; Mondelli, C.; Schmidt, T.; Schlüter, O. F.-K.; Wolf, A.; Mleczko, L.; Dreier, T. *Energy Environ. Sci.* **2011**, *4*, 4786–4799.
- (2) Over, H.; Schomäcker, R. *ACS Catal.* **2013**, *3*, 1034–1046.
- (3) Crihan, D.; Knapp, M.; Zweidinger, S.; Lundgren, E.; Weststrate, C. J.; Andersen, J. N.; Seitsonen, A. P.; Over, H. *Angew. Chem., Int. Ed.* **2008**, *47*, 2131–2134.
- (4) López, N.; Gómez-Segura, J.; Marín, R. P.; Pérez-Ramírez, J. *J. Catal.* **2008**, *255*, 29–39.
- (5) Seki, K. *Catal. Surv. Asia* **2010**, *14*, 168–175.
- (6) Amrute, A. P.; Mondelli, C.; Schmidt, T.; Hauert, R.; Pérez-Ramírez, J. *ChemCatChem* **2013**, *5*, 748–756.
- (7) Mondelli, C.; Amrute, A. P.; Krumeich, F.; Schmidt, T.; Pérez-Ramírez, J. *ChemCatChem* **2011**, *3*, 657–660.
- (8) Amrute, A. P.; Krumeich, F.; Mondelli, C.; Pérez-Ramírez, J. *Chem. Sci.* **2013**, *4*, 2209–2217.
- (9) Wolf, A.; Mleczko, L.; Schlüter, O. F.-K.; Schubert, S. US20110180419 A1, 2011.
- (10) Studt, F.; Abild-Pedersen, F.; Hansen, H. A.; Man, I. C.; Rossmeisl, J.; Bligaard, T. *ChemCatChem* **2010**, *2*, 98–102.
- (11) Kim, K. W.; Lee, E. H.; Kim, J. S.; Shin, K. H.; Jung, B. I. *Electrochim. Acta* **2002**, *47*, 2525–2531.
- (12) Tanuma, S.; Powell, C. J.; Penn, D. R. *Surf. Interface Anal.* **1994**, *21*, 165–176.
- (13) Yeh, J. J.; Lindau, I. *At. Data Nucl. Data Tables* **1985**, *32*, 1–155.
- (14) Mitchell, S.; Michels, N.-L.; Kunze, K.; Pérez-Ramírez, J. *Nat. Chem.* **2012**, *4*, 825–831.
- (15) Amrute, A. P.; Mondelli, C.; Pérez-Ramírez, J. *Catal. Sci. Technol.* **2012**, *2*, 2057–2065.
- (16) Kresse, G.; Furthmüller, J. *Comput. Mater. Sci.* **1996**, *6*, 15–50.
- (17) Kresse, G.; Furthmüller, J. *Phys. Rev. B* **1996**, *54*, 11169–11186.
- (18) Hammer, B.; Hansen, L. B.; Nørskov, J. K. *Phys. Rev. B* **1999**, *59*, 7413–7421.
- (19) Blöchl, P. E. *Phys. Rev. B* **1994**, *50*, 17953–17979.
- (20) Monkhurst, H. J.; Pack, J. D. *Phys. Rev. B* **1976**, *13*, 5188–5192.
- (21) Henkelman, G.; Uberuaga, B. P.; Jónsson, H. *J. Chem. Phys.* **2000**, *113*, 9901–9904.
- (22) Wulff, G. Z. *Kristallogr. Mineral.* **1901**, *34*, 449–530.
- (23) Novell-Leruth, G.; Carchini, G.; López, N. *J. Chem. Phys.* **2013**, *138*, No. 194706.
- (24) Teschner, D.; Farra, R.; Yao, L.-D.; Schlögl, R.; Soerijanto, H.; Schomäcker, R.; Schmidt, T.; Szentmiklósi, L.; Amrute, A. P.; Mondelli, C.; Pérez-Ramírez, J.; Novell-Leruth, G.; López, N. *J. Catal.* **2012**, *285*, 273–284.
- (25) Wertheim, G. K.; Guggenheim, H. *J. Phys. Rev. B* **1980**, *22*, 4680–4683.
- (26) Peuckert, M. *Surf. Sci.* **1984**, *144*, 451–464.
- (27) Folkesson, B. *Acta Chem. Scand.* **1973**, *27*, 287–302.
- (28) Zweidinger, S.; Crihan, D.; Knapp, M.; Hofmann, J. P.; Seitsonen, A. P.; Weststrate, C. J.; Lundgren, E.; Andersen, J. N.; Over, H. *J. Phys. Chem. C* **2008**, *112*, 9966–9969.
- (29) The energy for  $\text{Cl}_2$  evolution obtained in our study corresponds to ca. 3 eV. This value is similar to the estimation in ref 10, as elimination of the gas-phase entropy contribution from their energy data reported in this article leads to 2.7 eV.
- (30) Greenwood, N. N.; Earnshaw, A. *Chemistry of the Elements*; Elsevier: Oxford, U.K., 2008; pp 1079 and 1117.
- (31) Kondratenko, E. V.; Amrute, A. P.; Pohl, M.-M.; Steinfeldt, N.; Mondelli, C.; Pérez-Ramírez, J. *Catal. Sci. Technol.* **2013**, *3*, 2555–2558.
- (32) Hevia, M. A. G.; Amrute, A. P.; Schmidt, T.; Pérez-Ramírez, J. *J. Catal.* **2010**, *276*, 141–151.
- (33) Seitsonen, A. P.; Over, H. *J. Phys. Chem. C* **2010**, *114*, 22624–22629.
- (34) Jitianu, M.; Ko, J. K.; Miller, S.; Rohn, C.; Haber, R. A. *Ceram. Trans.* **2010**, *223*, 87–99.
- (35) Shay, D. T. WO2011075277A1, 2011.
- (36) Mitchell, S.; Michels, N.-L.; Pérez-Ramírez, J. *Chem. Soc. Rev.* **2013**, *42*, 6094–6112.